Electronic Supplementary Material (ESI) for Nanoscale.
This journal is © The Royal Society of Chemistry 2020

Electronic Supplementary Material (ESI) for Nanoscale. This journal is © The Royal Society of Chemistry 2020

Electronic Supplementary Information

Tuning epitaxial growth on $NaYbF_4$ upconversion nanoparticles by strain management

*Jianxiong Zhao, Bing Chen, Xian Chen, Xin Zhang, Tianying Sun, Dong Su, and Feng Wang**

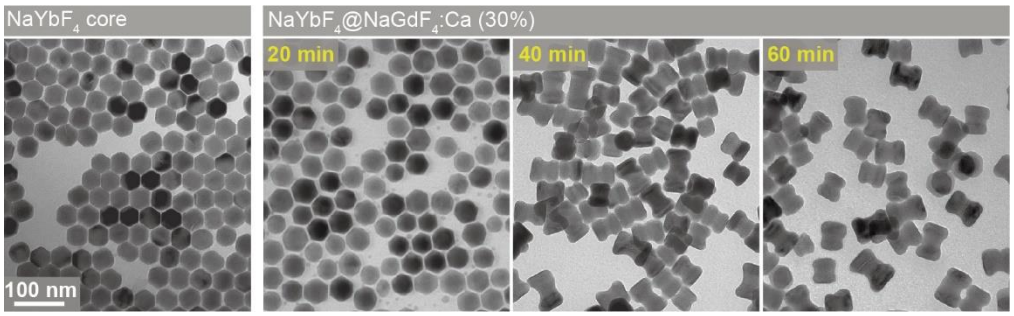

Figure S1. TEM images of the $NaYbF_4$@$NaGdF_4$:Ca (30%) nanoparticles at different stages of the synthesis, showing the decomposition of the lateral shell and eventual formation of dumbbell-like nanostructures. Spherical nanoparticles were used as the core.

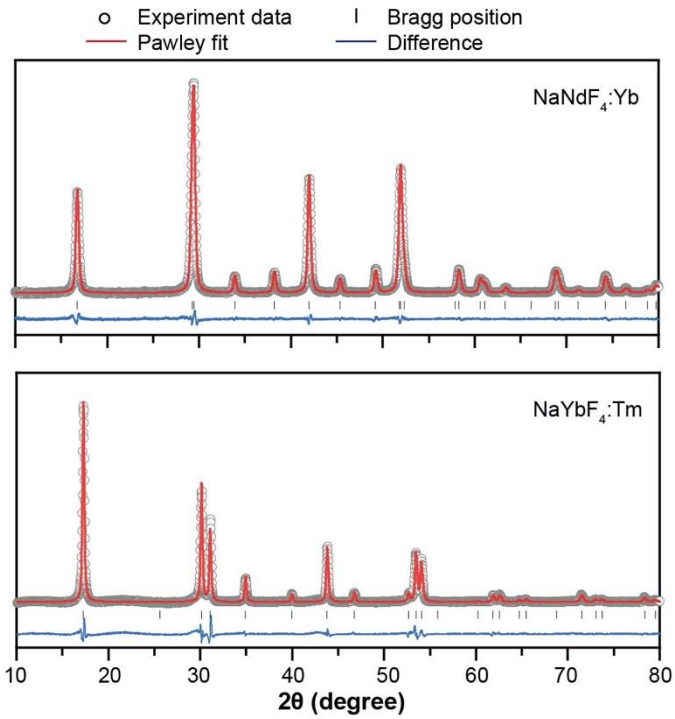

Figure S2. XRD patterns and Pawley Fit of the $NaNdF_4$:Yb (10%) and $NaYbF_4$:Tm (1%) nanoparticles. The fitting was performed using the TOPAS 4.2 program.

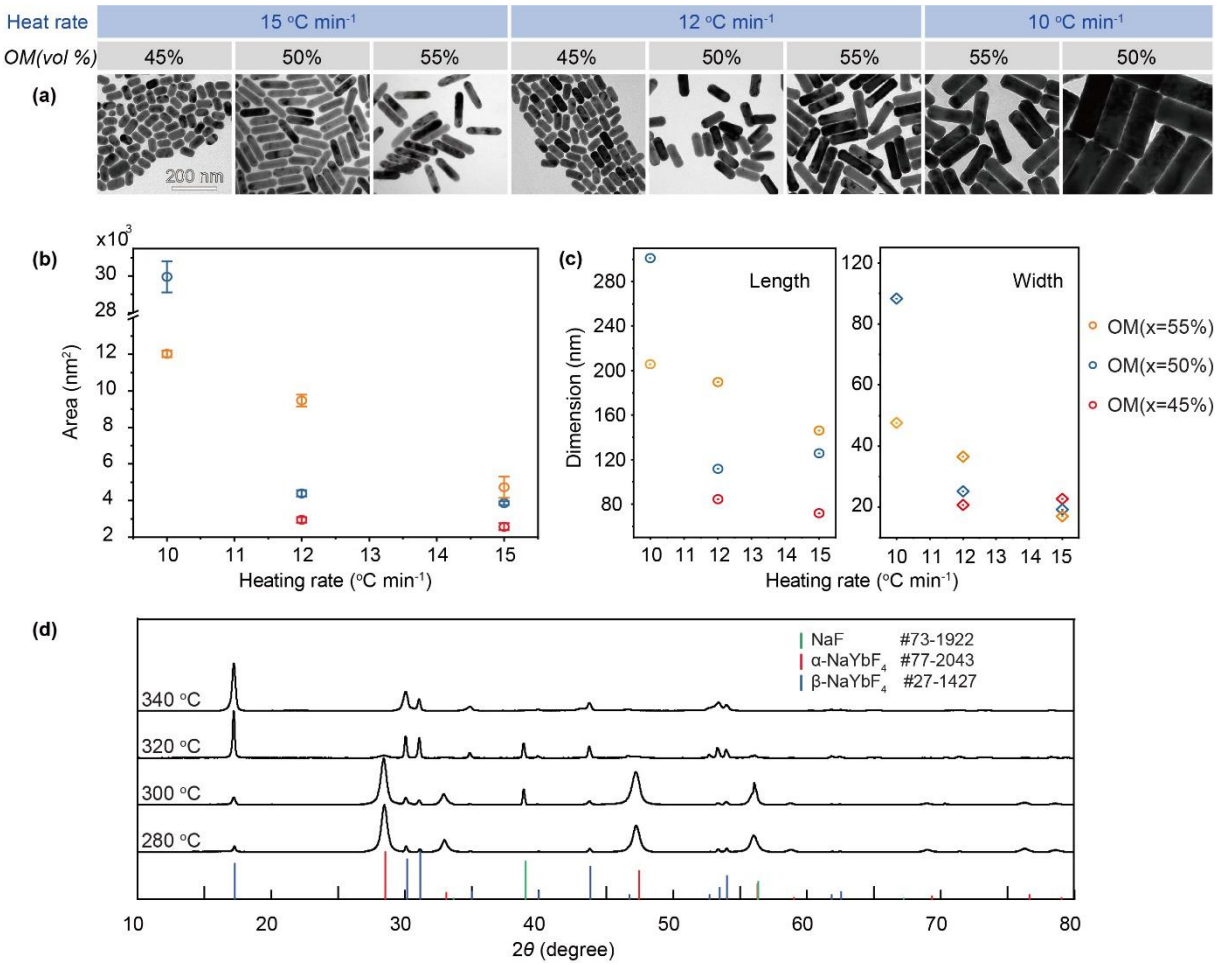

Figure S3. (a) TEM images of the $NaYbF_4$ nanoparticles synthesized under different experimental conditions. (b, c) The statistics on particle area and shape factors (length and width) of the nanoparticles in (a). In our experiment, we synthesized the $NaYbF_4$ nanoparticle by using a solvent mixture of OM/OA/ODE (volume ratio: *x*/1-*x*/1) at three different heat rates of 15 °C min^{-1}, 12 °C min^{-1}, and 10 °C min^{-1}, respectively. The heating rates and solvent compositions collectively regulate the nucleation and phase transition kinetics that result in the size and shape control.[S1-S3] (d) XRD patterns of the samples synthesized at different temperatures. The heating rate was fixed at 12 °C min^{-1} and the OM content was fixed at 55%. The results showed that a high reaction temperature of 340 °C was needed to obtain the pure hexagonal phase $NaYbF_4$.

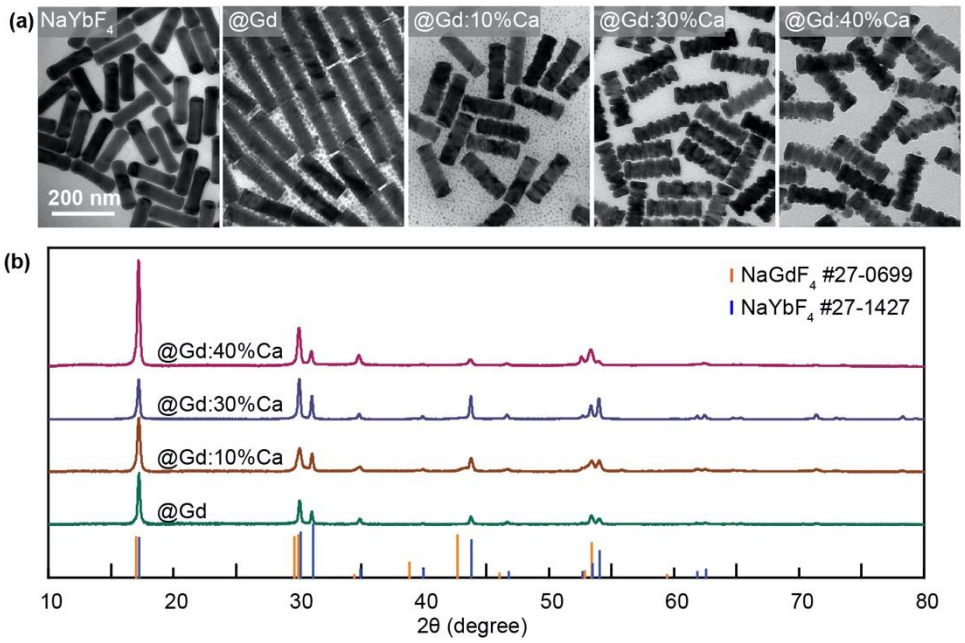

Figure S4. (a) TEM images and (b) XRD patterns of $NaYbF_4$@$NaGdF_4$:Ca nanoparticles as a function of Ca^{2+} concentration in the shell layer. The introduction of Ca^{2+} dopant leads to a high local concentration of precursor and an effective relaxation of strain in shell lattice, thereby promoting the epitaxial process. At low Ca^{2+} concentrations (i.e.; 0%, 10%, and 20%), the relatively large residual strain in the shell hindered the deposition of part of the shell precursors on the core by heterogeneous nucleation. Small nanoparticles were thus formed due to the homogeneous nucleation of gadolinium precursors. At an optimal Ca^{2+} concentration of 30%, uniform $NaYbF_4$@$NaGdF_4$:Ca ribbed nanorods were formed. Because the activation energy for both homogeneous and heterogeneous growth decreased with increasing local precursor concentration, an over high Ca^{2+} doping level (i.e.; 40%) prompted fast self-nucleation and formation of isolate $NaGdF_4$:Ca nanoparticles. XRD results in (b) show that all the nanoparticles were crystallized in the hexagonal phase.

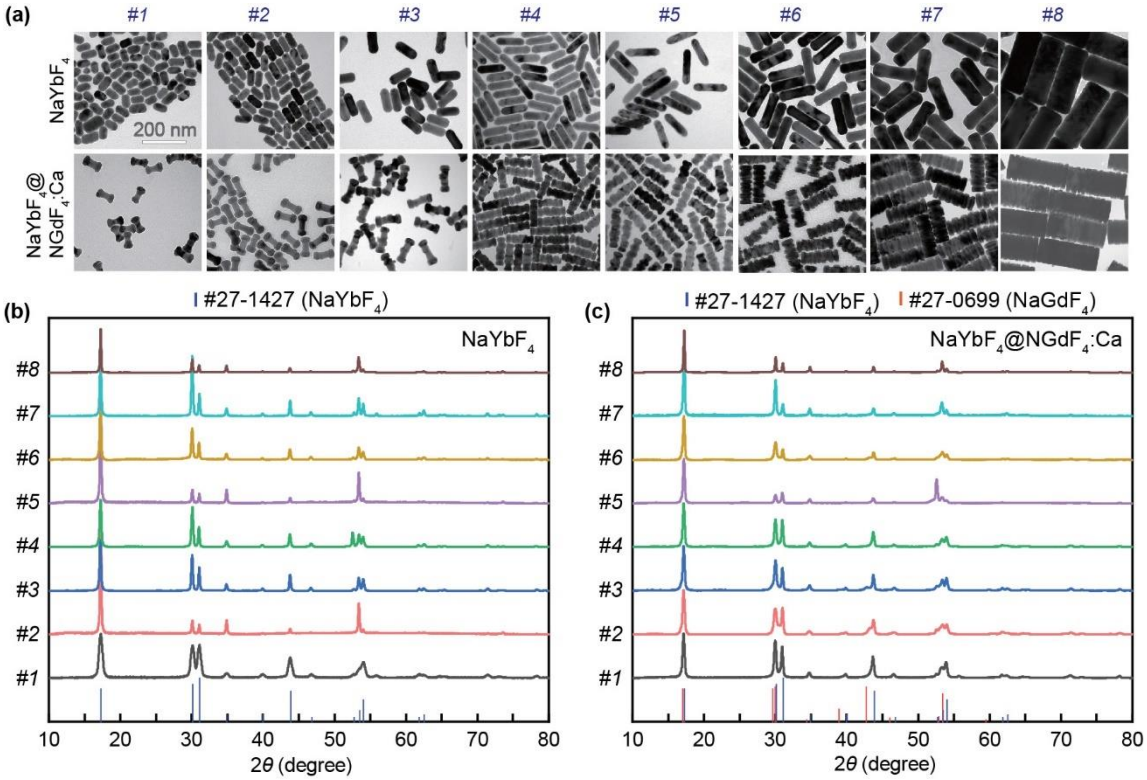

Figure S5. (a) TEM image of $NaYbF_4$ core and $NaYbF_4$@$NaGdF_4$:Ca (30%) core–shell nanoparticles in our study. (b)XRD patterns of the corresponding samples. The patterns with number #1–8 from bottom to top is corresponding to the TEM image in (a) from left to right.

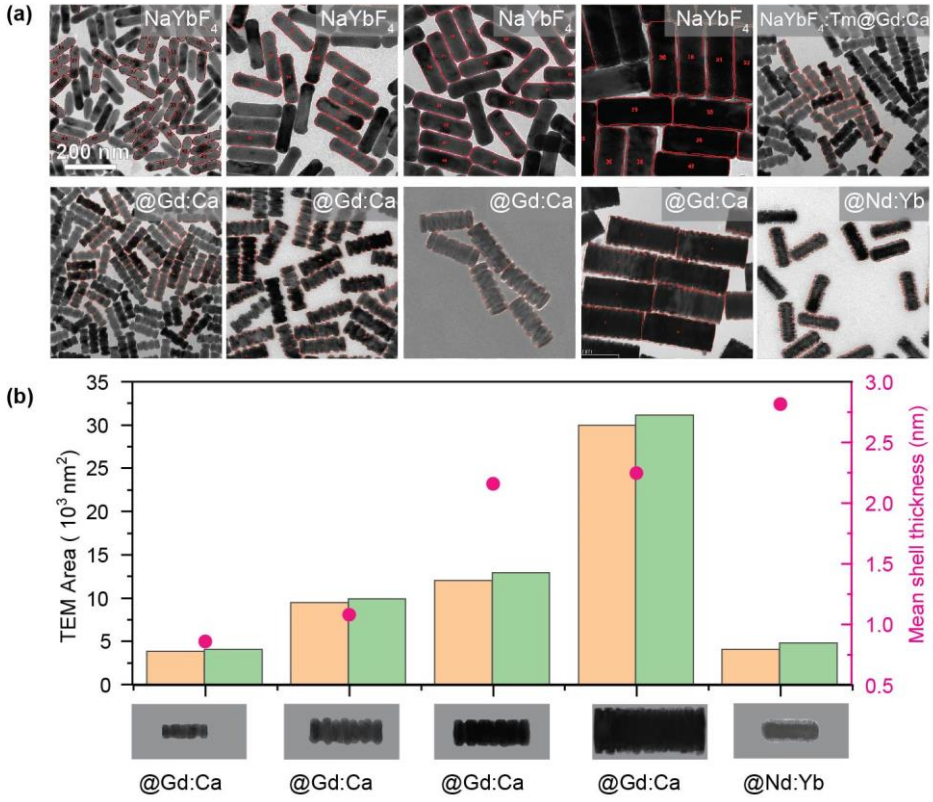

Figure S6. Estimation of the shell coverage on the lateral surface of the core nanorod. The mean particle areas of the core and core/shell particles were calculated by using the FIJI program.[S4] (a) The image processing for the area calculation on core and core/shell TEM image. (b) The comparison of the nanoparticle areas and the mean shell thickness for different nanostructures. The mean shell thickness was calculated by equation S3.

$$Mean\ shell\ thickness = \frac{Core/shell\ area - Core\ area}{Core\ nanorod\ perimeter} \qquad (S3)$$

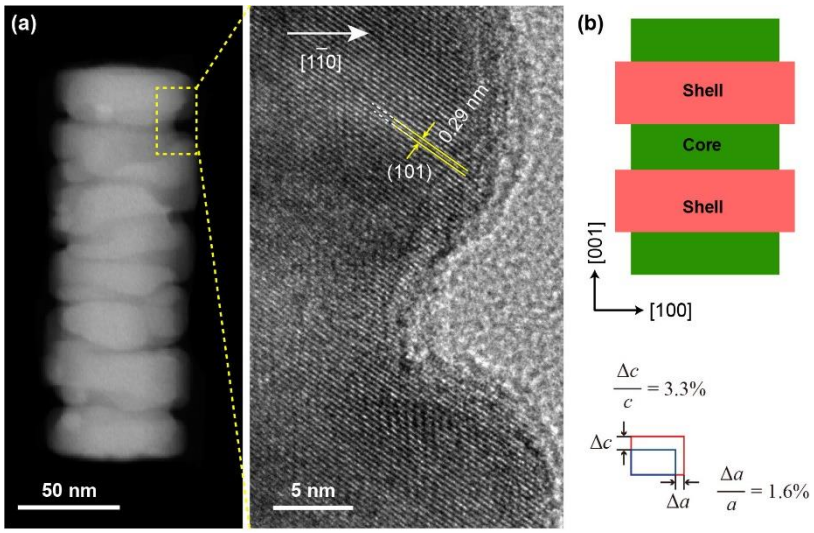

Figure S7. (a) HAADF-STEM and high-resolution TEM images of the $NaYbF_4$@$NaGdF_4$:Ca (30%) core–shell nanoparticles showing the preferential shell growth in the <100> directions. (b) Misfit parameters for the epitaxial growth in the [100] and [001] directions on the prism facet. The island-like shell featured preferential growth in the [100] direction due to the relatively small lattice mismatch.

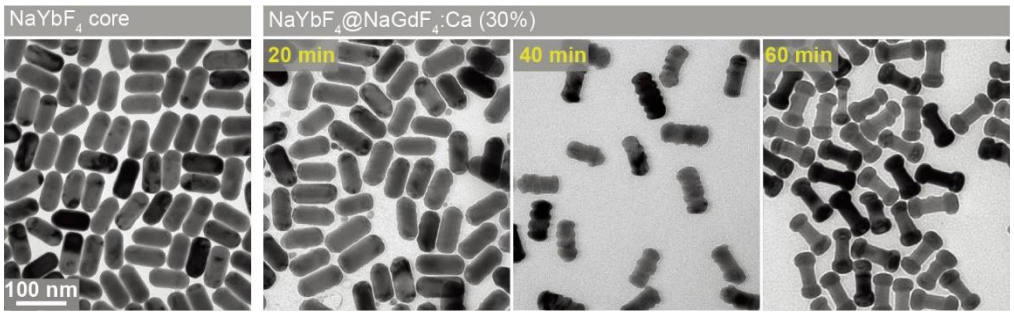

Figure S8. TEM images of the $NaYbF_4$@$NaGdF_4$:Ca (30%) nanoparticles at different stages of the synthesis, showing the decomposition of the lateral shell and eventual formation of dumbbell-like nanostructures. Short nanorods were used as the core.

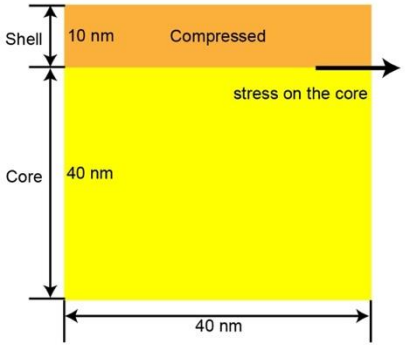

Figure S9. The schematic of the nanorod section bending by misfit stress. The bending induced strain relaxation is demonstrated by investigating the deformation of the beam in the 2D lattice. Assuming that the core (thickness *r*, lattice parameter a_1) and shell layer (thickness *t*, lattice parameter a_2) is elastically isotropic and shares the same elastic modulus but different lattice parameter (**Table S1**). The core layer is subject to tensile stress applied by the mismatched shell layer. If the core and shell layers are uniformly strained without bending, the strain magnitude is calculated by equation S4 and S5.

$$\varepsilon_{core} = |\frac{a_1 r + a_2 t}{r+t} - a_1|/a_1 \quad \text{(S4)}$$

$$\varepsilon_{shell} = |a_2 - \frac{a_1 r + a_2 t}{r+t}|/a_2 \quad \text{(S4)}$$

When strain in the shell layer is accumulated on one side only, the non-uniformly distributed stress can bend the beam.[S5] The displacement fields are described by equation S6 and S7 (*x* and *y* are coordinated with the origin at nanorod section center:

$$u_x = \frac{M}{EI}|xy| \quad \text{(S6)}$$

$$u_y = -\frac{M}{2EI}(x^2 + \nu y^2) \quad \text{(S7)}$$

where *M* is torque, *E* is Young's modulus, *I* is the polar moment of inertia, and *v* is the Poisson ratio. The magnitude of strain in the *x* and *y* directions are:

$$\varepsilon_{xx} = \frac{\partial u_x}{\partial x}$$

$$\varepsilon_{yy} = \frac{\partial u_y}{\partial y}$$

The curvature of the beam is estimated by Equation (S8):

$$\kappa = \frac{M}{EI} \quad \text{(S8)}$$

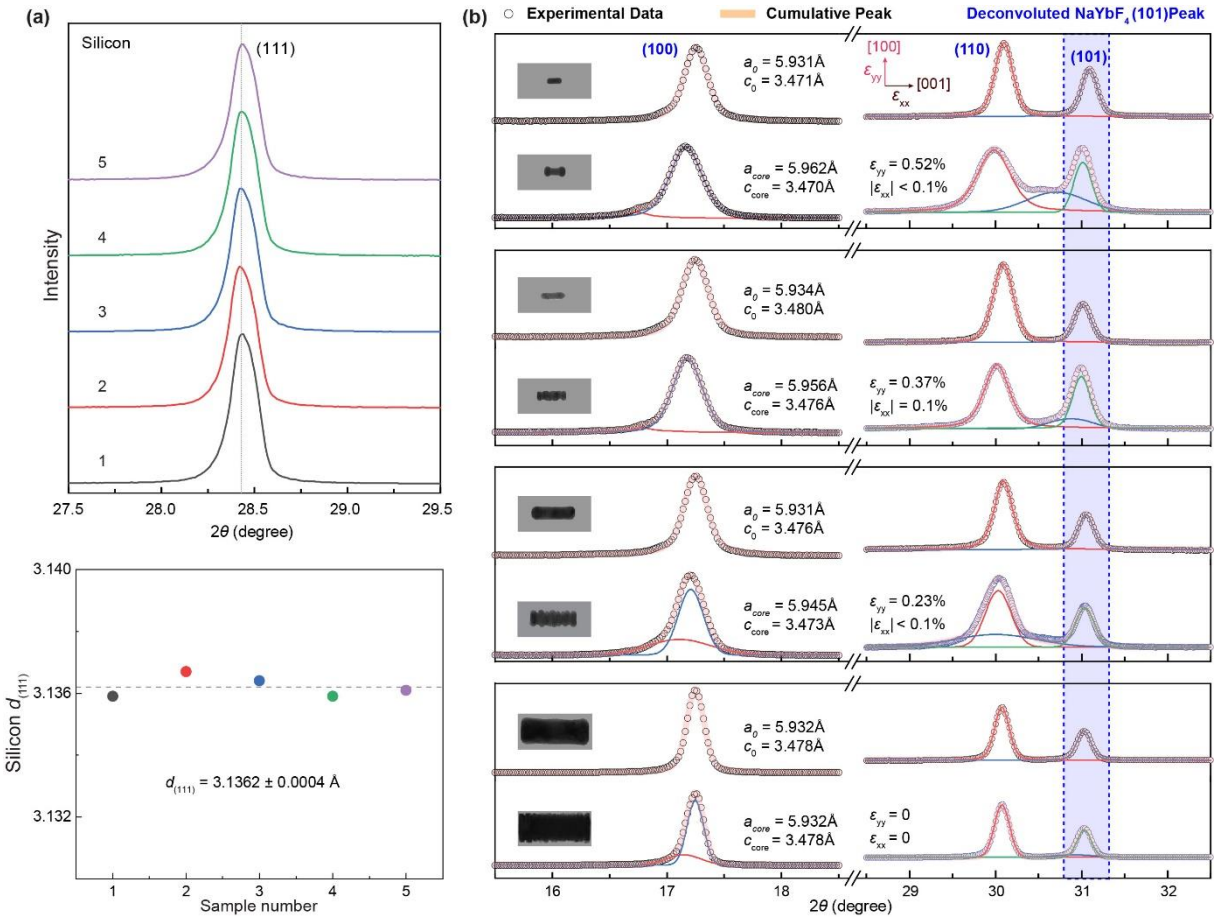

Figure S10. (a) Evaluation of the error of *d*-spacing measurement using five replicates of silicon powder samples. The sample alignment was conducted for each measurement to eliminate the error caused by the deviation in sample thickness. The pseudo-Voigt function fit on the peak was used to calculate the (111) *d*-spacing. The calculated standard deviation was as small as 4×10^{-4} Å. (b) XRD patterns of the $NaYbF_4$ core and $NaYbF_4$@$NaGdF_4$:Ca (30%) core–shell nanoparticles fitted by the Pseudo-Voigt function. Inset: TEM images of corresponding nanoparticles. The unstrained lattice parameter (a_0) and strained core lattice parameter (a_{core}) were calculated based on the major peak position of the (100) planes. The unstrained lattice parameter (c_0) and strained core lattice parameter (c_{core}) were calculated based on the major peak position of the (101) planes together with the calculated a_0 and a_{core} values. The strain in the core was estimated by equations S1 and S2:

$$\varepsilon_{xx} = \frac{|c_{\text{core}} - c_0|}{c_0} \qquad (S1)$$

$$\varepsilon_{yy} = \frac{|a_{\text{core}} - a_0|}{a_0} \qquad (S2)$$

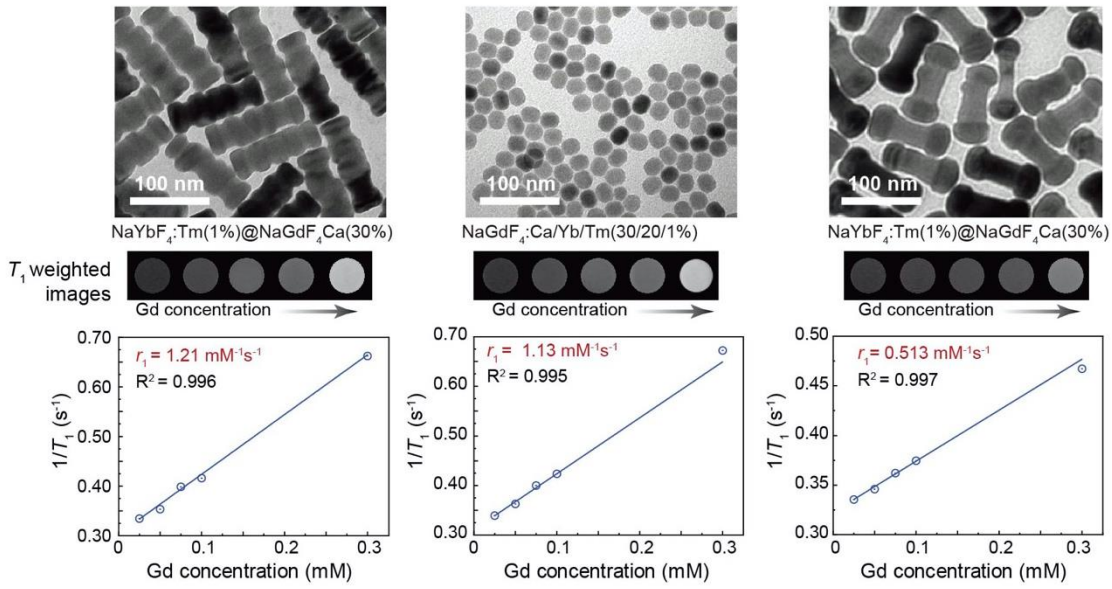

Figure S11. The T_1 ionic relaxivity plotted against the molar concentration of Gd^{3+} for poly ethylenimine (PEI) coated $NaGdF_4$:Ca/Yb/Tm (30/20/1%) nanoparticles and $NaYbF_4$:Tm (1%)@$NaGdF_4$:Ca (30%) nanoparticles of different morphologies at a magnetic field of 3T. Ionic relaxivity r_1 (mM^{-1} s^{-1}) was determined by the slope of the linear fit.

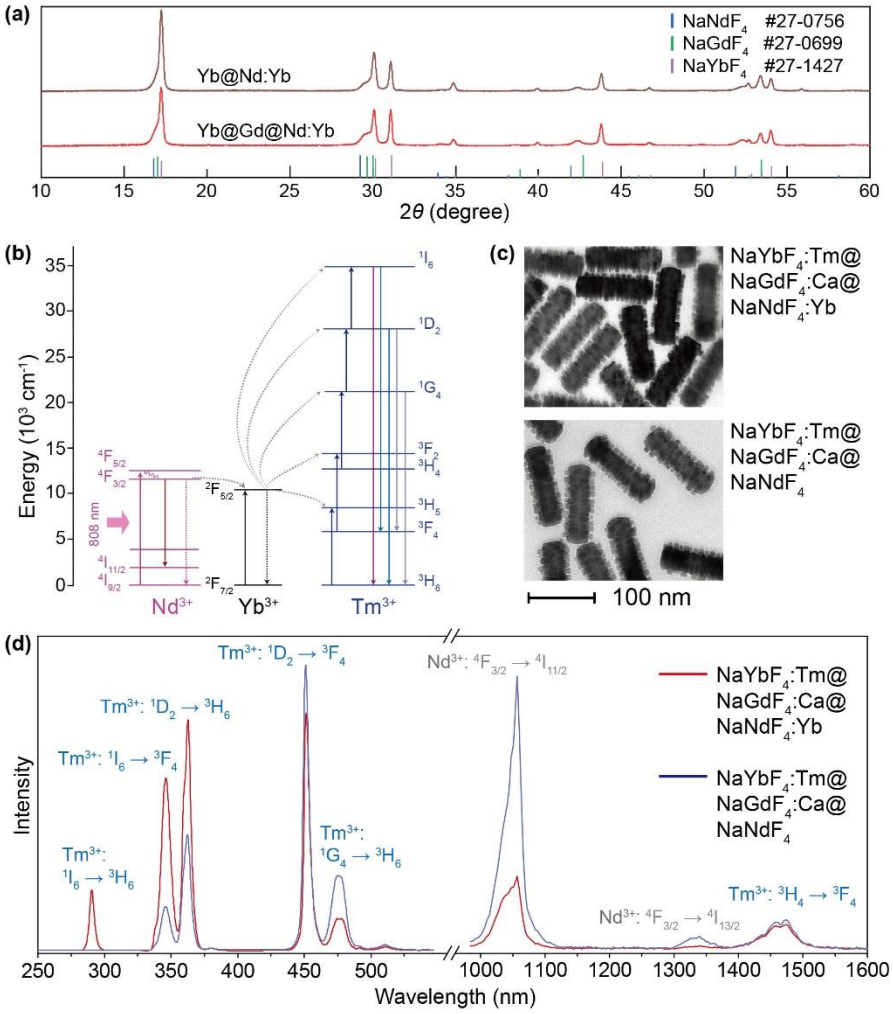

Figure S12. (a) XRD patterns of the $NaYbF_4$:Tm (1%)@$NaGdF_4$:Ca (30%)@$NaNdF_4$:Yb (10%) and the $NaYbF_4$:Tm (1%)@$NaNdF_4$:Yb (10%) nanoparticles, showing the pure hexagonal phase. (b) Simplified energy diagram showing the proposed upconversion process sensitized by Nd^{3+}. (c) TEM images of the $NaYbF_4$:Tm (1%)@$NaGdF_4$:Ca (30%)@$NaNdF_4$:Yb (10%) and the $NaYbF_4$:Tm (1%)@$NaGdF_4$:Ca (30%)@$NaNdF_4$ nanoparticles, showing the similar size and morphology. (d) Emission spectra of the nanoparticles in (c) under 808 nm excitation. The presence of Yb^{3+} dopants in the $NaNdF_4$ shell promotes energy transfer to the core layer by suppressing radiative recombination in the Nd^{3+} ions.

Table S1. Unstrained lattice parameter *a* and *c* for $NaLnF_4$ (Ln = lanthanide) derived from ref. [S6] or calculated by Pawley Fit of measured data in Figure S2.

Chemical Formula	**Lattice parameter *a* (Å)**	**Lattice parameter *c* (Å)**	**Source**
$NaYbF_4$	5.930	3.467	Ref. [S6]
$NaYbF_4$:Tm (1%)	5.931	3.471	Figure S2
$NaGdF_4$	6.038	3.595	Ref. [S6]
$NaGdF_4$:Ca (10%)	6.033	3.588	Ref. [S6]
$NaGdF_4$:Ca (20%)	6.027	3.585	Ref. [S6]
$NaGdF_4$:Ca (30%)	6.024	3.584	Ref. [S6]
$NaGdF_4$:Ca (40%)	6.020	3.581	Ref. [S6]
$NaNdF_4$:Yb (10%)	6.108	3.701	Figure S2

Table S2. The misfit parameter for different core/shell combinations. The misfit parameters were calculated based on Equation S9 and S10:

$$f_{\mathrm{a}} = \frac{|a_0 - a_1|}{a_0} \qquad \text{(S9)}$$

$$f_{\mathrm{l}} = \frac{|a_0 - a_1| + |c_0 - c_1|}{a_0 + c_0} \qquad \text{(S10)}$$

where a_0 and c_0 are the unstrained lattice parameters for the core and a_1 and c_1 are the unstrained lattice parameters for the shell.

Core	**Shell**	**Misfit f_{a} (%) (epitaxy on basal facets)**	**Misfit f_{l} (%) (epitaxy on prism facets)**
$NaYbF_4$	$NaGdF_4$	1.82%	2.51%
	$NaGdF_4$:Ca (10%)	1.73%	2.38%
	$NaGdF_4$:Ca (20%)	1.63%	2.29%
	$NaGdF_4$:Ca (30%)	1.58%	2.24%
	$NaGdF_4$:Ca (40%)	1.51%	2.17%
$NaYbF_4$:Tm (1%)	$NaGdF_4$:Ca (30%)	1.57%	2.19%
	$NaNdF_4$:Yb (10%)	2.98%	4.32%

References

S1. Sharifi Dehsari, H.; Heidari, M.; Halda Ribeiro, A.; Tremel, W.; Jakob, G.; Donadio, D.; Potestio, R.; Asadi, K. Combined Experimental and Theoretical Investigation of Heating Rate on Growth of Iron Oxide Nanoparticles. *Chem. Mater.* **2017**, 29, 9648-9656.

S2. Bu, W.; Chen, Z.; Chen, F.; Shi, J. Oleic Acid/Oleylamine Cooperative-Controlled Crystallization Mechanism for Monodisperse Tetragonal Bipyramid $NaLa(MoO_4)_2$ Nanocrystals. *J. Phys. Chem. C* **2009**, 113, 12176-12185.

S3. Chen, B.; Kong, W.; Wang, N.; Zhu, G.; Wang, F. Oleylamine-Mediated Synthesis of Small $NaYbF_4$ Nanoparticles with Tunable Size. *Chem. Mater.* **2019**, 31, 4779-4786.

S4. Schindelin, J.; Arganda-Carreras, I.; Frise, E.; Kaynig, V.; Longair, M.; Pietzsch, T.; Preibisch, S.; Rueden, C.; Saalfeld, S.; Schmid, B.; Tinevez, J. Y.; White, D. J.; Hartenstein, V.; Eliceiri, K.; Tomancak, P.; Cardona A. Fiji: an Open-Source Platform for Biological-Image Analysis. *Nat. Methods* **2012**, 9, 676-682.

S5. Cleland, A. N. Foundations of Nanomechanics: from Solid-State Theory to Device Applications. Springer Science & Business Media, 2013.

S6. Zhao, J.; Chen, X.; Chen, B.; Luo, X.; Sun, T.; Zhang, W.; Wang, C.; Lin, J.; Su, D.; Qiao, X.; Wang, F. Accurate Control of Core–Shell Upconversion Nanoparticles through Anisotropic Strain Engineering. *Adv. Func. Mater*. **2019**, 29, 1903295.